Materials Characterization 172 (2021) 110877

Contents lists available at ScienceDirect

Materials Characterization

journal homepage: www.elsevier.com/locate/matchar

Lattice distortion as an estimator of solid solution strengthening in high-entropy alloys

Ankit Roy [a], Praveen Sreeramagiri [a], Tomas Babuska [a], Brandon Krick [a], Pratik K. Ray [b], Ganesh Balasubramanian [a,*]

[a] Department of Mechanical Engineering & Mechanics, Lehigh University, Bethlehem, PA 18015, USA
[b] Department of Metallurgical & Materials Engineering, Indian Institute of Technology, Ropar, Punjab 140001, India

ARTICLE INFO

Keywords:
High-entropy alloys
Hardness
Young's modulus
Lattice strain
Solid-solution strengthening
Cohesive energy

ABSTRACT

Over the past decade, select high-entropy alloys (HEAs) have exhibited excellent structural properties, even at high temperatures, outperforming conventional alloys in some cases. Intriguingly, some reports in the literature suggest that HEA properties may be enhanced by increasing the number of elements, while another school of thought negates this notion and suggests that there is no clear dependence of mechanical properties on number of elements. We further examine this question in the context of a quinary refractory alloy system (MoTaTiWZr) and scrutinize whether number of elements in a HEA positively impact its mechanical properties. The present work showcases that certain equiatomic low- and medium- entropy alloys can exhibit superior structural properties (hardness, Young's modulus) relative to their higher-entropy counterparts composed of the same family of elements. Evidently, incorporating a higher number of constituent elements does not guarantee enhanced structural properties. Using a synergy of experimental measurements, complementary microscopic characterization and materials theory, we conclusively demonstrate that the intrinsic lattice distortion and cohesive energies are the predominant strengthening mechanisms that are reflected as high hardness and Young's moduli of single-phase multicomponent alloys investigated in this work. Severe lattice distortion is one of the core effects of HEAs which imparts excellent room temperature structural properties and is generated by mixing multiple atom types. Likewise, a higher cohesive energy between the atoms in a lattice requires greater shear stresses to break the metallic bonds that increases the stiffness. An alloy with lower number of elements may intrinsically possess a higher cohesive energy than one with a higher number of elements within the same series, thereby outperforming the higher-entropy alloy on the structural properties.

1. Introduction

The exponentially increasing interest in high-entropy alloys (HEAs) is attributed to their outstanding structural properties such as ultra-high hardness [1–3], excellent high temperature strength [4], and notable resistance to surface oxidation [5] and corrosion [6,7]. Common routes for synthesis of HEAs at the lab scale include arc melting [8], mechanical alloying and spark plasma sintering (MA + SPS) [9] and reduction of oxide powder precursor mix [10]. The common strengthening mechanisms in HEAs are tangled dislocations, mechanical twinning, secondary phase particles and dislocation pinning by solute atoms [9] that cause serrated flow during mechanical deformation [11] in HEAs. However, it is not clear what is the extent to which entropy directly affects these properties. The underlying physical principles that govern the mechanical properties of these alloys remain an area of active research, with one school of thought [12,13] proposing number of elements as a major influence, while another perspective [8,14] partially negates this. Fig. 15 in Ref. [12] shows an increase in yield strength, ductility and ultimate tensile strength with the increase in number of elements in the Co-Cr-Fe-Mn-Ni alloy series. The author cites a higher degree of solid solution strengthening as the underlying cause for this phenomenon. Likewise, Fig. 4 in Ref. [13] shows that the stacking fault energy reduces as the number of elements increase in NiFeCrCoMn alloy series, thereby evincing improved ductility with an increase in the number of elements. Contrary to these findings, Wu et al. [14] investigated the FeNiCoCrMn alloy to study the effect of number and type of alloying elements on the mechanical properties of the alloys, and found that simply adding more elements does not increase the hardness of the alloys. Though these two

* Corresponding author at: Packard Laboratory 561, 19 Memorial Drive West, Bethlehem, PA 18015, USA.
E-mail address: bganesh@lehigh.edu (G. Balasubramanian).

https://doi.org/10.1016/j.matchar.2021.110877
Received 4 August 2020; Received in revised form 26 December 2020; Accepted 1 January 2021
Available online 6 January 2021

studies do not weigh the same mechanical property, they do, however, conclude a positive and neutral impact of increasing the number of elements in a HEA, respectively, that do not concur with each other. Adding more elements increases the entropy of the system which was originally cited as the underlying principle that stabilizes the single-phase in these alloys and prevents the formation of compounds [1].

Though other research efforts do not directly establish that a higher number of elements enhances alloy properties, the findings do indicate a positive effect of having a greater number of elements. Salishchev et al. [15] studied the effect of Mn and V addition in HEAs and their results showed that the hardness increases from 160 HV in CoCrFeNi to 524 HV in CoCrFeNiV, and further increases to 650 HV in CoCrFeNiMnV. In another work, Zhang et al. [16] investigated the effect of mixing a third element in binary Ti—22Nb alloy and found that adding Fe or Mo to TiNb alloys increases the yield strength to twice the value and also increases the elastic modulus by ~20%.

Thus, the question whether entropy plays a role in determining the mechanical properties of HEAs has equivocal views in the literature, with a fairly large part of the community establishing that entropy has no role in determining the mechanical properties. In this paper, we attempt to address this dichotomy and corroborate that the effect of entropy is minimal, if not negligible. To assess the trends in mechanical properties that exist for HEAs, we collect hardness and elastic modulus data from our previous work [17]. Table S1 of supplementary information lists the hardness values of 127 alloys and Table S2 provides the Young's modulus of 84 alloys obtained from literature. We offer this data as a step to contribute to the data-analytics enabled mechanical property predictions for HEAs. Fig. 1(a) reproduces the Young's modulus values of all 84 alloys and Fig. 1(b) presents the hardness of 127 alloys, both as a function of the number of elements. Clearly, no evident dependence of these mechanical properties on the number of elements is noted.

Therefore, we shift our focus to investigate the fundamental causes for enhanced mechanical properties in HEAs. Murty et al. [18] cited four core effects that distinguish HEAs from conventional alloys viz., the high entropy of mixing, severe lattice distortion, sluggish diffusion and cocktail effect. The high entropy of mixing in HEAs compensates for the enthalpy of formation, thereby preventing the growth of compounds and favoring the single-phase crystallographic configuration [1]. The sluggish diffusion effect imparts excellent creep resistance to HEAs [19]. The first notable study that investigated the sluggish diffusion phenomenon in HEAs was carried out by Tsai et al. [20] and they showed that the activation energy for diffusion (Q) normalized by the HEA melting temperature (T_m) are higher for metals in a HEA matrix than in the pure state, thus proving that diffusion is sluggish in HEAs. This concept was challenged by the argument that the values of diffusion seem to be retarded only when normalized by the T_m and hence the findings are still considered inconclusive [21]. But another notable work supporting the occurrence of sluggish diffusion used the concept of reduced diffusion coefficients to successfully show that diffusion can indeed be shown to be retarded in HEAs [22]. The lattice distortion is known to cause strain in the HEA lattice thereby imparting room temperature resistance to deformation [23]. The cocktail effect is known to blend in desirable properties as per the preferences of the alloy designer [18]. Other approaches to enhance the structural properties of HEAs include doping the alloys with oxygen [24], precipitation hardening [25], and synthesizing eutectic HEAs with alternating hard/soft BCC/FCC phases to enhance strength and ductility [26]. The exceptional room temperature structural properties are conjectured to arise due to the non-uniformity in the lattice introduced by the presence of multiple atom types that warp the crystal lattice. This extreme chemical disorder in the lattice contributes to solid-solution hardening [1]. However, addition of multiple (> 4) principal elements in equivalent proportions (a.k.a. high entropy configuration) does not solely guarantee enhanced structural properties for HEAs [1,8,14] as discussed previously. A recent report computationally designed and experimentally validated a stable non-equiatomic composition $(Mo_{0.95}W_{0.05})_{0.85}Ta_{0.10}(TiZr)_{0.05}$ with 5 refractory metals, that exhibited superior tensile and compressive strength relative to the equiatomic high-entropy counterpart, as well commercial Mo-rich alloys [27]. We use the binary, ternary, quaternary and quinary subsytems from the MoTaTiWZr alloy series for investigation in this work as the alloys obtained by combining these elements cover all major types of crystal structures. We correlate hardness (H) and Young's modulus (E) with the resistance to localized plastic deformation and cohesive energy respectively, using theoretical formulations and also using experimental methods. High hardness materials are particularly important in metal working industry for cutting various hard materials for instance alloy steels and high-speed tool steels [28]. At the atomic level, elastic strain manifests itself as minute changes in interatomic bond lengths. Therefore, the modulus of elasticity (E) is a measure of the interatomic bonding forces. In fact, when atoms occupy the equilibrium position, E is directly proportional to the slope of the interatomic force separation curve [29]. A material with high E requires a high load to overcome elastic deformation and cause permanent deformation. Fig. 2 (a) (details are provided in Table S3 as supplementary information) shows certain low- and medium-entropy alloys possess higher hardness and Young's modulus relative to the high-entropy solid-solutions [17]. Hence, one can assert that the underlying mechanisms that impart outstanding structural properties to some of these complex concentrated alloys over others, is rooted to causes beyond just the number of principal elements in a HEA, contrasting with the results of Fig. 15 in ref. [12]. Here, we conclusively prove that lattice distortion is the

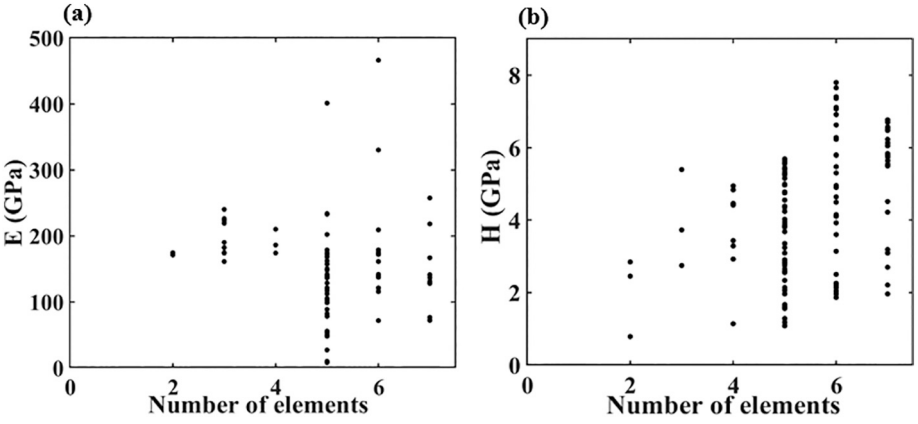

Fig. 1. Mechanical properties as a function of number of elements in a HEA. (a) Young's modulus vs. number of elements for 127 HEAs and (b) Hardness vs. number of elements for 84 HEAs. Clearly, no dependence of mechanical properties on number of elements is seen ruling out the idea that simple elemental addition might improve mechanical performance of these HEAs.

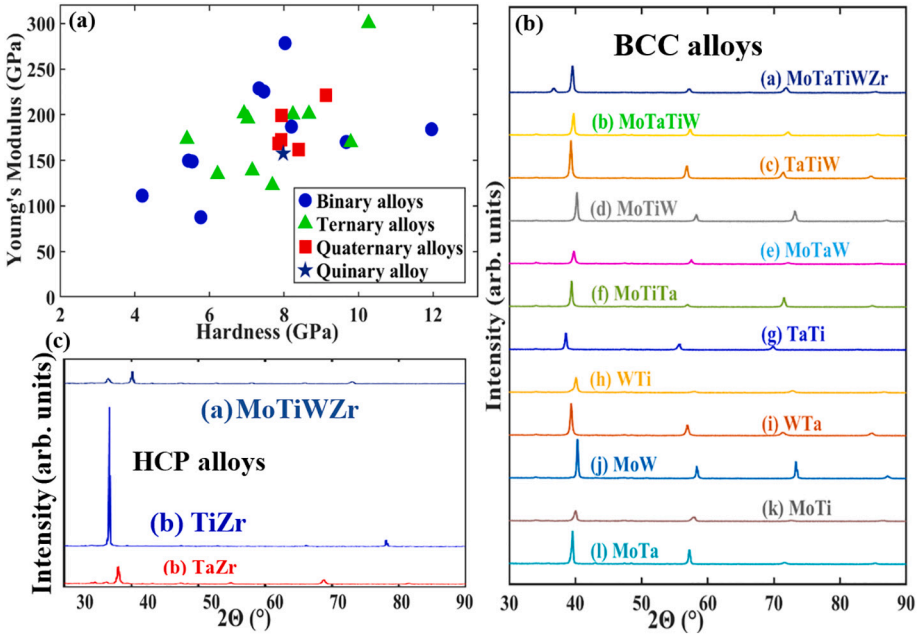

Fig. 2. Structural properties and crystallographic phases of binary, ternary, quaternary and quinary multicomponent alloys. (a) Variation of Young's modulus (E) and hardness presented for 26 equiatomic multicomponent alloys composed of refractory metals Mo-Ta-Ti-W-Zr. Note that the binary (blue circles) and ternary alloys (green triangles) outperform the quaternary alloys (red squares). The quinary alloy (purple star) has relatively moderate E and hardness, thus corroborating that impact of the number of elements in an equiatomic multicomponent alloy is minimal on the structural properties. XRD patterns of the 15 single-phase equiatomic alloys in the as cast condition (the remaining 11 alloys exhibit multiple phases and hence not considered in the present study) are presented in (b) (12 BCC alloys) and (c) (3 HCP alloys). As pure metals, Mo and W intrinsically form a BCC structure, while Ti and Zr crystallize as HCP at room temperature. Ta exhibits both BCC and tetragonal phases. Hence, interestingly, all binaries except two form a single-phase structure conforming with the Hume-Rothery rules (alloys with Zr form HCP while others form BCC). Owing to its large atomic radius, Zr increases the atomic size difference δ between the elements of the alloy, and decreases the possibility of forming a single-phase solid-solution. The presence of Ti, drives the lattice formation of Zr containing single-phase ternary and quaternary alloys to the HCP configurations, resulting in an intrinsically closed packed crystal structure. (For interpretation of the references to color in this figure legend, the reader is referred to the web version of this article.)

driving factor that predominantly contributes to the high hardness (H) of multicomponent alloys, while cohesive energy predominantly determines stiffness or elastic modulus (E). Configurational entropy simply facilitates the classification of these alloys into bands that demonstrate linear correlation between E and the corresponding cohesive energy. These findings are elaborated in the succeeding sections.

2. Methods

2.1. Sample preparation

All possible equiatomic binary, ternary, quaternary and quinary alloys composed of refractory metals Mo-Ta-Ti-W-Zr are synthesized by arc-melting using elemental powders (Sigma-Aldrich, purity $\geq$99.9%; $<$ 45 μm mean particle size) in an argon atmosphere at a pressure of 30 psi, on a copper hearth with water cooling. Powdered metals reduce the possibility of macro-segregation and improve compositional homogeneity throughout the alloy sample. Powders are mixed thoroughly in a laboratory jar mill (Thomas Scientific Series 8000), at an optimum rotational speed to maintain a balance between the impact of the gravitational and centrifugal forces on the powder mixture being rotated. Next, the mixture is compressed in a Carver hydraulic press up to a pressure of 5000 psi to form cylindrical pellets of diameter 20 mm. The compressed pellets are arc-melted (Edmund Bühler GmbH Mini Arc Melting System MAM1) on a water-cooled copper hearth, and re-melted repeatedly for a total of four times to ensure enhanced homogeneity. The samples are hot mounted (Buehler SimpliMet 4000 Mounting Press) and polished with several grit papers ranging from 120 to 600, followed by ~20 μm suspended diamond paste.

2.2. Microstructural characterization

X-ray diffraction (Panalytical Empyrean vs. 7.9f 20,170,530) in a Bragg-Brentano geometry using Cu-Kα radiation ($\lambda = 0.154$ nm, 45 kV, 40 mA) is utilized for identifying the crystallographic phases with the 2θ scan in the range of 10 to 90 degrees. The phases are analyzed using a Malvern Panalytical HighScore software package [30]. A Hysitron TI900 nanoindenter with a Berkovich tip is used for the nanoindentation measurements on mounted and polished samples. Indents are performed with load control and a maximum load of 5 mN, and a 5–2–5 s load-hold-unload profile. An array of 25 indents (5 × 5 pattern) spaced 10 μm apart along the x and y directions is executed on each sample, while the structural properties are evaluated using the Oliver-Pharr method [31]. To investigate the microstructures of the samples, the polished samples are chemically etched in a solution of 1:1:4 hydrofluoric acid (HF), nitric acid (HNO_3) and water respectively for 5–10 s. A comparatively concentrated solution is used to account for the high corrosive resistance of various samples. Microstructures of the samples are visualized and analyzed using Scanning Electron Microscope (SEM) and Energy Dispersive X-Ray Spectroscopy (EDS). Secondary electron (SE) images and X-ray intensity maps using energy-dispersive spectroscopy (EDS) are obtained on a HITACHI S-4300SE/N SEM operated at an accelerating voltage of 20 kV with beam current of 3 nA. An Everhart-Thornley detector and an EDAX Octane Elect Plus detector are used for recording the SE images and X-ray EDS compositional maps, respectively. The data is exported using the EDAX Genesis software.

3. Results

All possible equiatomic binary, ternary, quaternary and quinary alloys composed of refractory metals Mo-Ta-Ti-W-Zr are synthesized by arc-melting and their hardness and Young's moduli measured by nanoindentation. The X-ray diffraction patterns of the as cast alloys, presented in Figs. 2 (b)-(c), reveal that six of the ten binary alloys, four of the ten ternary, one of the five quaternary, and the sole quinary alloy exhibit BCC peaks, while two of the binary and one of the quaternary alloys forms an HCP phase. Details are provided in Table S3 as supplementary information. The microstructure of two ternary alloys with

widely differing strength and hardness, viz., MoTaTi (with a relatively low hardness of 5.4 GPa and low E = 173 GPa) and MoTaW (with relatively high hardness 10.27 GPa and high E = 300 GPa) are further characterized using a scanning electron microscope (SEM). Secondary electron images as shown in Figs. 3(a) and (e), and the compositional color mapping images reproduced in Figs. 3(b-d) and Figs. 3(f-h) using energy dispersive X-ray spectroscopy (EDS) corroborate that the microstructures are predominantly dendritic. The dendrites of MoTaTi are rich in Ta (Fig. 3 (c)) although the inter-dendritic regions are rich in Ti (Fig. 3 (d)), and we find Mo to be distributed uniformly in both regions (Fig. 3 (b)). This segregation may be avoided by homogenization but since our primary intention is to study the properties and state of alloys in the as-cast condition after crystallization, we do not carry out further heat treatment. The Ta rich phase is a bcc solid solution of high melting elements and is expected to have a higher melting temperature as compared to the Ti rich phase. Hence, the primary solidifying dendritic phase is the Ta rich phase and the Ti rich regions are formed in the inter-dendritic regions. Mo and Ta have similar crystal structures and form a continuous solid solution [32] with relatively strong inter-atomic bonds [33]. On the other hand, Ti has a hcp structure and shows limited solid solubility in either Mo [32] or Ta [32], which is probably the reason for its segregation into the inter-dendritic regions. For MoTaW, a uniform distribution is noted, as expected intuitively, for all the constituent elements (Figs. 3 (f-h)) because all three binaries – MoW, MoTa and TaW are isomorphous systems with similar crystal structures forming continuous solid solution across the phase diagram with relatively strong interatomic bonding [33], and the three elements exist *sans* segregation and forms a solid solution with an equiaxed microstructure upon casting, as seen in Fig. 3 (e). The above observations are further corroborated by the line profile in Fig. 3 (i) where Ti concentration rises steeply in the inter-dendritic region of MoTaTi, whereas such drastic fluctuations are absent in MoTaW (Fig. 3 (j)). Thus, the superior structural properties of MoTaW relative to MoTaTi may be conjectured to arise from elemental segregation in the latter alloy. Additionally, one can note that elemental W has a higher elastic modulus than Ti, which likely contributes to the higher elastic modulus of the alloy.

Amongst the refractory metals, Mo and W crystallize into the BCC structure, while Ti and Zr assume a HCP lattice at room temperature and BCC allotropes at elevated temperatures (1155 K for Ti [34] and 1138 K for Zr [35]). Likewise, Ta exhibits two crystallographic phases viz., BCC and tetragonal (transformation temperature = 755–775 °C) [36]. For the equiatomic binary alloys composed of these five elements, all but two form a single-phase solid-solution in accord with the Hume-Rothery guidelines. Interestingly, Ti forms a single-phase solid-solution when

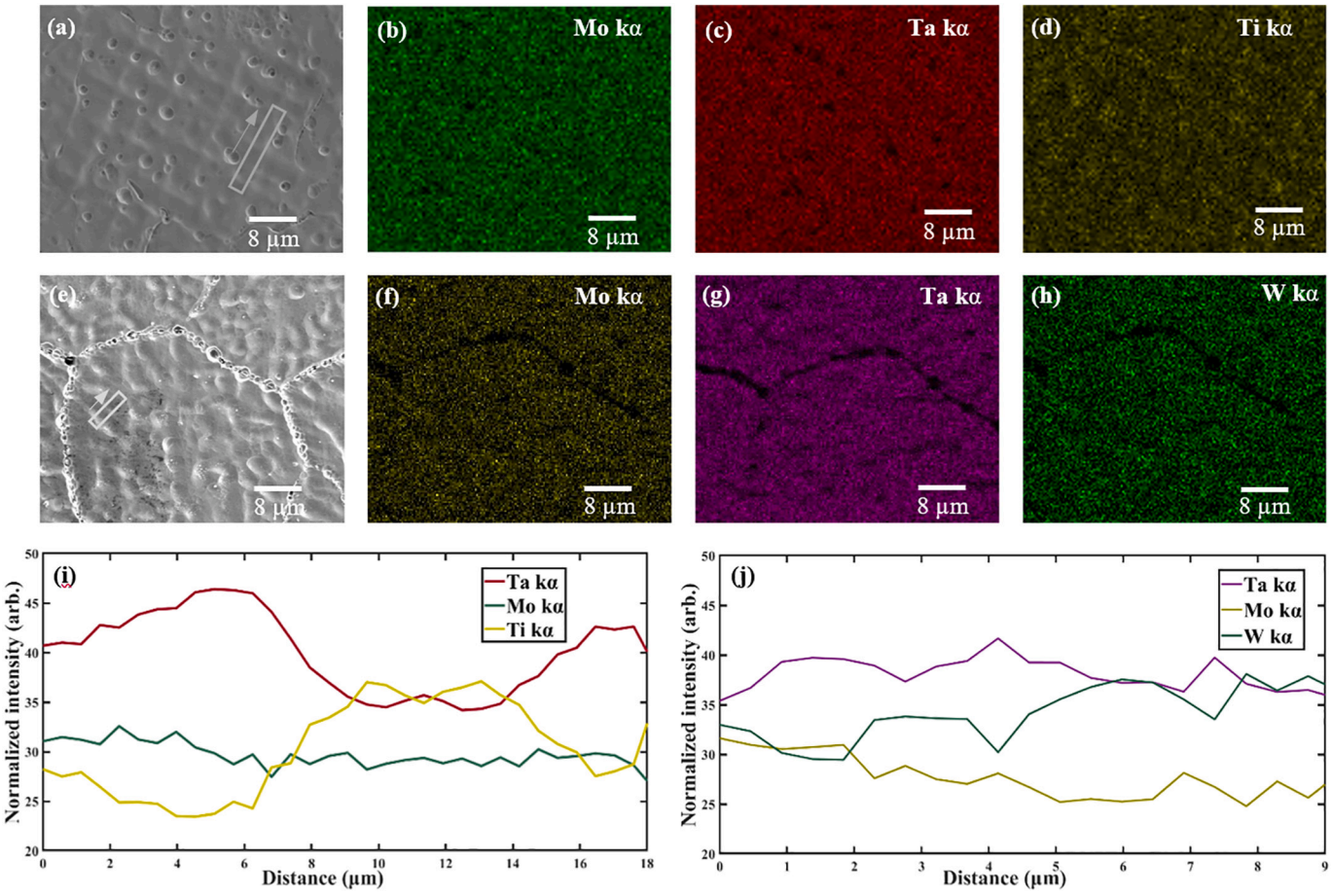

Fig. 3. Scanning electron microscope (SEM) micrographs of ternary equiatomic multicomponent alloys. (a-d) MoTaTi (E = 173 GPa) and (e-h) MoTaW (E = 300 GPa), both in the as-cast condition and synthesized by arc-melting. A dendritic microstructure is noted for both the alloys. Energy-dispersive spectroscopy (EDS) performed on the microstructures with X-ray intensity maps of individual elements: (b) Mo kα, (c) Ta kα, (d) Ti kα are the X-ray signals for MoTaTi, and (f) Mo kα, (g) Ta kα, (h) W kα are the X-ray signals for MoTaW. Quantitative elemental mapping in EDS converts X-ray counts into numerical composition values. (i) and (j) are the line profiles obtained from (a) and (e), and illustrate the normalized intensities of X-ray signals of the individual elements in both alloys. Both line profiles based on SE images correspond well with thickness of dendritic region ~6 μm and inter-dendritic region ~7 μm for the case of MoTaTi. In MoTaTi, the interdendritic regions are rich in Ti (as indicated by the drastic rise in Ti concentration in (i)) and deficient in Ta, while Mo is uniformly distributed throughout. In MoTaW, all constituent elements show a uniform distribution thus justifying the superior structural properties in comparison to MoTaTi where elemental segregation degrades the elastic property of the alloy.

alloyed with the other four elements, but Zr forms multi-phase compounds with mixed with BCC elements (Mo and W). This behavior can be attributed to the greater mismatch in atomic radius between the elements, with Zr being significantly larger than the other atoms. A similar trend is observed in ternary alloys, where the addition of Zr destabilizes the single-phase lattice structure. The atomic size difference $\delta = \sqrt{\sum_{i=1}^{n} C_i\left(1-\frac{r_i}{\bar{r}}\right)^2}$ [37] explains this observation (Table S3), where C_i is the concentration of each elemental component, r_i is the atomic radius of each metal and r is the mean radius of the alloying elements. Alloys containing Zr attain a relatively higher $\delta > \sim 4\%$ and do not form a BCC phase and show a tendency to transition to multiphase, with the exception of the quinary alloy where the other four metals diminish the effect of δ. However, the presence of Zr in quaternary alloys results in the formation of multiple crystallographic phases in three of the four possible compositions. A caveat associated with the δ parameter used in this work is that it considers the usage of atomic radii from standard elemental tables [38]. Egami et al. [39] demonstrated that the elemental radii change when they are alloyed in the form of metallic glasses. This was found to be especially prominent in metal-metalloid systems. For example, the radius of Ni is 1.246 Å in its pure form [40] but changes to 1.28 Å when present in Ni75P25 [39]. Similarly, Chen et al. [40] emphasized that the binding state of each species in the HEA matrix is different which alters the actual atomic radius. To obtain to experimental radius of each element as present in the alloy matrix, they synthesized a series of 9 NbMoCrTiAl alloys (all BCC) while changing the concentrations of Nb and Cr, and obtained the actual mean atomic radius of the alloy $\bar{r}_j = \frac{\sqrt{3}}{4} a_j^{bcc}$, by calculating the lattice parameter a_j^{bcc} from XRD, where suffix j represents each of the 9 alloys. Further they used the Vegard's rule $\sum_{i=1}^{n} x_i r_i = \bar{r}_j$, where n is total number of elements in the alloy and r_i is the radius of each metal, on all 9 compositions to obtain the individual radius of each element as present in the alloy matrix. The approach addresses the need to account for volume shifts during alloying. While this method is quite rational in its approach, it is applicable only on an alloy series where the elements in every alloy are same but there proportions are varied. This is because the solution of $\sum_{i=1}^{n} x_i r_i = \bar{r}_j$ equation requires $i \leq j$ or, to solve this equation for obtaining r_i, we need to have an alloy series where each alloy contains same elements but in different proportions but the number of alloys is larger than or equal to the number of elements used in each alloy. Interestingly, the radii of elements (whose original crystal structure is same as that of the alloy) obtained by this method were almost identical to the radii of elements in the pure form. This confirms the absence of charge transfer effects in a scenario where non-metals are absent and the differences in electronegativities are relatively small. In the present work we study 26 different alloys that can be made by all possible combinations of Mo, Ta, Ti, W and Zr elements. Since the elements in each alloy varies we cannot use the approach described above. In this work we investigate alloys that contain only early transition-metals and hence we neglect the charge transfer effects that cause the change of radius in metals. Therefore, we assume the theoretical δ, that uses standard atomic radii of metals in the pure state, to be a reasonable accurate indicator of the phases. Moreover, the theoretical δ calculated by using radii of metals as that in pure state, has previously been used to predict solid solution phases in HEAs. Zhang et al. [41] investigated the TiZrNbMoVx and CoCrFeNiAlNbx alloys and found that for the formation of single-phase solid solution, $\delta \leq 6.6\%$. This findings of their work supports our case of using δ calculated by using the pure state metal radii. Alongside δ, we adopt two additional parameters to predict the formation of solid solution alloys. We use the atomic packing factor γ, from ref. [42] to predict solid solution formation, which is calculated by using $\gamma = \left(1-\sqrt{\frac{(r_s+\bar{r})^2-\bar{r}^2}{(r_s+\bar{r})^2}}\right) \Big/ \left(1-\sqrt{\frac{(r_L+\bar{r})^2-\bar{r}^2}{(r_L+\bar{r})^2}}\right)$, where r_S and r_L are the radii of the smallest and the largest atoms and $\bar{r}$ is the mean radius. The values of γ for all 26 alloys are tabulated in Table S3 and compared with δ in Fig. S2 (a). As ref. [42] mentions, we see roughly a single phase solid solution formation when $\gamma < 1.175$. Also, $\delta \sim 6\%$ roughly demarcates the transition from single phase to multiphase in the alloys investigated in this work which is close to the value mentioned in a prior report [41]. There are a few outliers using both δ and γ but the overall efficiency in distinguishing solid solutions from multiphase alloys appears to be identical. We calculate another term called the displacement parameter, α_2 [43], which is formulated as $\alpha_2 = \sum_{j \geq i}^{n} \frac{c_i c_j |r_i + r_j - 2\bar{r}|}{2\bar{r}}$, to separate the alloy phases. It is to be noted that α_2 is mathematically zero for binary alloys as the sum of the radius of two atom types *i* and *j* would be equal to twice that of the mean radius. Hence we could calculate α_2 for the remaining 16 alloys and the values are tabulated in Table S3 and compared with δ in Fig. S2 (b). The authors of ref. [43] did not demarcate a specific value of α_2 for the transition from single to multiphase but in the present work, a rough boundary exists at $0.006 < \alpha_2 < 0.007$ where $0.007 < \alpha_2$ gives multiphase and $\alpha_2 < 0.006$ results in single phase alloys.

Now, under an applied strain, the hardness (*H*) reflects the ability to resist localized plastic deformation, which is determined by the interaction energy of the solute atom with the dislocation, before the gliding takes place [44,45]. When a solute atom with an atomic size different than the host atom, is introduced in a lattice, it induces a stress field in its surroundings due to the resulting local dilation or constriction of the lattice. The interaction of these stress fields with the dislocations give rise to a solute atom-dislocation interaction energy (U_{size}) which is negative when the solute is smaller than the host (implying attraction towards a solute atom) and is given by the equation $U_{size} = \frac{4(1+\nu)Gbr^3\varepsilon_b \sin\theta}{3(1-\nu)R}$ [46], where G is the shear modulus, b is the burger vector, R is the distance between the solute atom and dislocation core, θ is the angle between the slip direction and the line joining the solute atom and dislocation core, r is the solvent atomic radius and $r(1+\varepsilon_b)$is the solute atom radius with $\varepsilon_b = \frac{1}{a}\frac{da}{dc}$ where a is the lattice parameter and c is the solute concentration and ν is the Poisson's ratio. While in most cases the stress field is spherically symmetric, some interstitials (point) defects in BCC lattices also produce tetragonal stress field. The interaction energy of dislocations with such tetragonal stress fields is larger than that of spherical stress fields and hence it is regarded as a hard obstacle [46]. To calculate the maximum U_{size}, b can be substituted with R, $\sin\theta = 1$ and ε_b as the fractional change in lattice parameter with fractional change in solute concentration [46]. We use ν as 0.3 for all cases as a generalization and choose the smallest atom as the solvent in the system [47]. Table S4 lists the calculated values of U_{size} and Fig. 4 shows reasonable dependence of hardness on U_{size}. The binary BCC alloys (shown in black

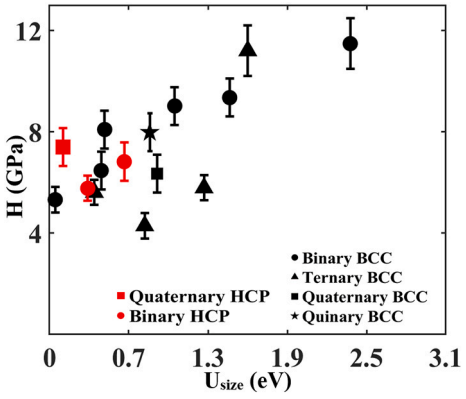

Fig. 4. Hardness (*H*) as a function of the solute atom-dislocation interaction energy (Usize) for single-phase multicomponent alloys. Binary BCC alloys show good fit of hardness with U_{size}. The U_{size} determines the resistance to dislocation motion due to the presence of solutes and higher value of U_{size} would result in higher H.

circles) show reliable linear trend with the quinary alloy and two binary HCP alloys fitting the trend well. We acknowledge the inability of the mathematical formulation of U_{size} to perfectly predict the hardening effects in our experiments and hence there are a few outliers viz. a viz. the ternary BCC. Apart from the sizes of solute atoms, the shear modulus (G) of solute atoms also dominate strengthening. An atom with lower G (soft atom) attracts a dislocation while an atom with higher G (hard atom) repels the dislocation [48]. Analogous to the size effect, the interaction energy formulation due to modulus effects is given by $U_{modulus} = \frac{G\varepsilon_G b^2 r^3}{(1-\nu)6\pi R^2(1+0.5|\varepsilon_G|)}$ [49], where $\varepsilon_G = \frac{1}{G}\frac{dG}{dc}$. The total interaction energy is the summation of the contributions of the 2 effects i.e. $U=U_{size} + U_{modulus}$. This U is primarily the energy barrier associated with the translation of a dislocation by a unit burger vector. We assert that higher the U, higher will be the energy barrier required for dislocation to propagate and higher will be the resistance to plastic deformation. Thus, a higher U (increased solid solution strengthening) in a HEA will result in higher hardness (H). There are many other factors that contribute to strengthening like electrical and chemical factors and it is reasonable to say that it is difficult to quantify the net strengthening through one single formulation because every aforementioned factor has a different variation with solute concentration [46]. To extend these formulations to HEAs poses a few major challenges. The traditional concept of solute and solvent does not apply to HEAs as there are multiple principal elements. Traditionally prior studies assume that solute is the largest atom in the alloy [47] but those studies were focused on alloys with only one or two major principal elements as the solvent. Also, even if the above mentioned formulations were modified and extended for HEAs as done for U_{size}, the calculation of ε_G to eventually calculate $U_{modulus}$ will be an arduous and time consuming experimental task as the variation of size and modulus effect will need to be studied with the change in concentration of every constituent element in the solvent lattice. Hence, the unavailability of required data to calculate $U_{modulus}$ limits the calculation of the total U. U_{size} alone is not sufficiently accurate in predicting the hardening effect and hence we see outliers in Fig. 4. To overcome these challenges we simplify the problem by stating that the degree of solid solution strengthening can be captured indirectly by measuring the lattice distortions existing in the lattices of HEAs [12,18]. This statement is consistent with the work of Owen et al. [23] who measured the lattice distortion in the CrMnFeCoNi in terms of the local lattice strain using the experimental pair distribution function (PDF) of HEAs. Another work (Fig. 5 in ref. [50]) emphasizes that the full width half maximum (FWHM) of Bragg peaks is a more accurate representation of the lattice distortions in HEAs rather than the PDF. Hence, we postulate that the quantification of lattice distortions by measuring the lattice strains using broadening of XRD Bragg peak (excluding the broadening caused by grain size) will reasonably represent the degree of solid solution strengthening.

Lattice distortion has been well described in the literature to cause impedance before dislocation motion begins [51,52] thereby reinstating the fact that a highly warped lattice will make the alloy harder than a lattice without distortion. Chen and Hendrickson observed that [45] indentation on an crystalline surface produces patterns of dislocations near the indents and the dislocation density changes as the depth of indentation changes. Pharr and Oliver [44] concluded that subsurface dislocation motions are responsible for the indentation plasticity and an increase in hardness would imply increase in difficulty of dislocation motion. By combining these findings we can safely establish that the lattice distortions, which determines resistance to dislocation motion, will sufficiently correlate with the measured hardness. Additionally, cohesive energy has also been cited as an important physical quantity to determine bond strength in the alloys, since bond strength is directly proportional to the resistance to deformation [53]. Hence, we correlate the lattice distortion and cohesive energies of the equiatomic alloys to their measured H and E values respectively to examine our hypothesis of high distortion resulting in high hardness and high cohesive energy resulting in high elastic modulus.

In a notable previous work, Yeh et al. [54] investigated a series of Cu-Ni-Al-Co-Cr-Fe-Si alloys and found the XRD peak intensities to reduce as the number of elements in the alloy was increased from 1 to 7. They

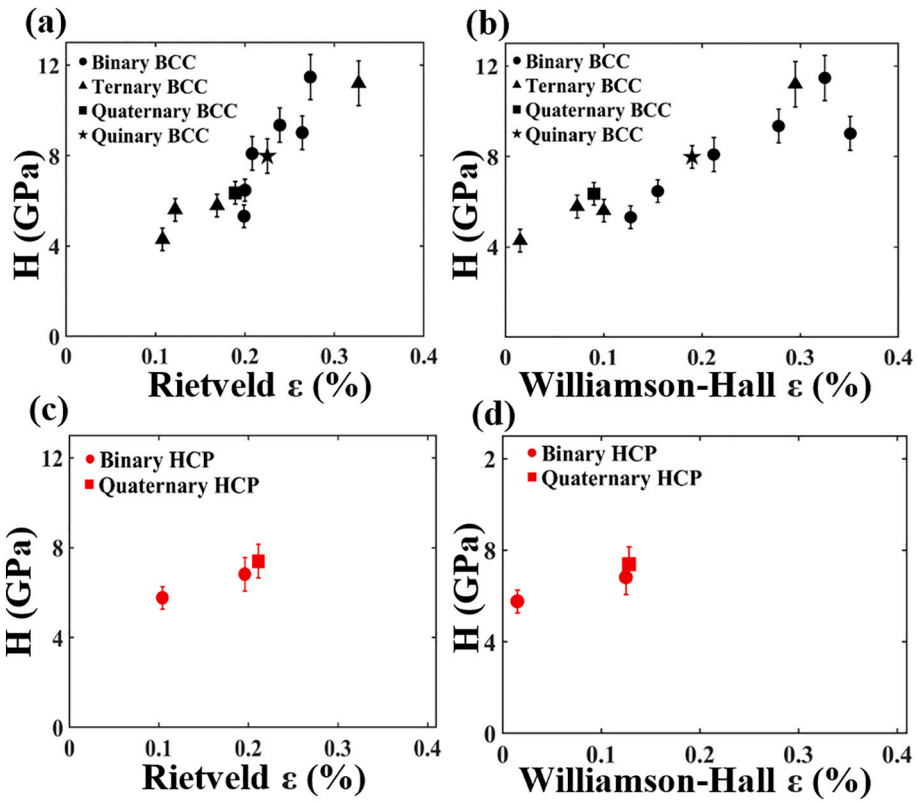

Fig. 5. Hardness (H) as a function of the lattice strain (ε) for single-phase multicomponent alloys. Lattice strains are calculated using (a) Rietveld refinement for BCC alloys, (b) W—H method for BCC alloys, (c) Rietveld refinement for HCP alloys, and (d) W—H method for HCP alloys. Results from both the methods reveal a predominantly linear correlation in both the BCC and HCP alloys, corroborating the significance of ε on the hardness. Although Rietveld in (a) and W—H method in (b) produce different values of ε for the same alloys owing to the sources of error involved in the respective methods, the underlying trend remains the same in both cases. For the HCP alloys, the linear variation between H and ε noted from both analyses ((c) and (d)) imply that higher lattice distortions contribute to an enhanced H by inducing solid-solution strengthening. The introduction of secondary and tertiary elemental species into the lattice of the base metal induces strain in the lattice which increases the resistance to plastic deformation.

attributed this reduction in XRD peak intensity to the loss of crystallization perfection caused by lattice distortion due to the presence of multiple atom species in the lattice. The authors were able to quantify intrinsic lattice distortion using the lattice constants obtained via XRD. In another noteworthy work, Praveen et al. [55] investigated the AlCoCrCuFe and NiCoCrCuFe alloys and calculated crystallite size and lattice strain from XRD patterns using the Williamson-Hall method. They found that spark plasma sintering causes a reduction in lattice strain from 1% to 0.2% in these alloys. Moreover, Naorem et al. [50] showed in their work that peak broadening in XRD is a true representation of bond length distortion. They concluded that this bond length distortion gives rise to lattice strain which can be accurately calculated by the experimentally obtainable quantity- FWHM. Hence, we use the XRD data from the experiments conducted in the present work to obtain the strains existing in the lattice of the alloys. We would like to stress that we are looking for trends in lattice distortion, as opposed to exact values. Therefore, one assumes while the actual values may show some changes, the trends will largely remain the same. In any case, we have used the smallest step-size of 0.0131° permissible in our equipment. Also, we emphasize that we intend to capture the uniform lattice distortion as explained in ref. [43] which can be measured by broadening of XRD peaks [56]. Having made this assumption, we adopt this technique to measure the strain in the lattice using our experimental XRD data. Two methods, viz., the Rietveld refinement [57] using MAUD [58] and the Williamson-Hall (W—H) technique [59] are employed to measure the lattice distortion as the lattice strain in each of the equiatomic solid-solutions.

In the Rietveld formulation, the experimental X-ray patterns of the synthesized alloys are fit to that of the phases, and the refinement of all parameters is performed iteratively by a least square method that effectively minimizes the residual parameter [57]. The Popa ($<\varepsilon^2>^{\frac{1}{2}}$, where ε is the crystal lattice strain) [60] and Delft models are used, and both render similar predictions (within 10% variation) for lattice strains. The goodness of fit (R_r) defined as the square of the ratio of weighted profile R-factor (R_{wp}) to the expected R factor (R_{exp}) [61] has been tabulated in Table S4 for all single-phase alloys and the values are comparable to those obtained for crystalline materials [62]. The dependence of H on Rietveld-refined strain is presented in Figs. 5 (a) and (c) (and details reported in Table S4 of supplementary information) for all the single-phase alloys suggests that lattice strain in a crystal exerts the predominant influence towards resisting plastic deformation.

Similar to Ref. [50] we employ peak broadening in XRD to obtain lattice distortions using lattice strain. Peak broadening in XRD occurs when the crystal structure deviates from the ideal configuration. These deviations might be due to the presence of dislocations, non-uniform lattice distortions or from solid-solution inhomogeneity. If the actual peak width is represented as β, then the observed peak width β_o can be expressed as a sum of peak broadening caused by the instrument and that due to strain and particle size, i.e.,

$$\beta_o = \beta_{ins} + \beta_{strain/crystallite}. \quad (1)$$

If β_{ins} is deducted from β_o, then the primary causes of peak broadening can be additively decoupled as those due to lattice strain and crystal size, as

$$\beta_{strain/crystallite} = \beta_{lattice\ strain} + \beta_{crystallite}. \quad (2)$$

Now, the Scherrer Eq. [63] states that $D = \frac{K\lambda}{\beta cos\theta} \Leftrightarrow \beta = \frac{K\lambda}{Dcos\theta}$, where D is the diameter of the grain, β is the peak width in radians at FWHM after subtracting β_{ins}, and $0.9 > K > 1$ depending on the shape of the grain. Hence,

$$\beta_{crystallite} = \frac{K\lambda}{Dcos\theta}. \quad (3)$$

Again, $\beta_{lattice\ strain} = 4\varepsilon \tan\theta$ represents the W—H uniform deformation model (UDM) [64], which assumes that all crystallographic directions have undergone an equal amount of strain [65].

Thus,

$$\beta_{strain/crystallite} = 4\varepsilon\, tan\theta + \frac{K\lambda}{Dcos\theta}, \quad (4)$$

or

$$\beta_{strain/crystallite}.cos\theta = 4\varepsilon\, sin\theta + \frac{K\lambda}{D}. \quad (5)$$

The considerable differences in the variation of $\beta_{strain/crystallite}.\cos\theta$ as a function of $\sin\theta$ (in Fig. S1 as supplementary information) for two representative alloys reveals the significant dissimilarities in the corresponding lattice strains, with a higher slope evincing the existence of a higher strain in the crystal. The R values of the fit of W—H plots for the single-phase alloys in this work have been tabulated as R_{WH} in Table S4. Nonetheless, both W—H (Figs. 5 (b) and (d)) and Rietveld methods reproduce similar predictions for lattice strains and corroborate that an increase in the lattice strain results in an increase in H of an equiatomic single-phase multicomponent alloy thereby affirming our hypothesis.

4. Discussion

The observed trends are strong manifestations of solid-solution strengthening. The presence of secondary and/or tertiary atoms enhances the distortion in the crystal lattice primarily due to atomic size mismatch, as well as due to differences in bonding energies [66–68]. This lattice distortion is accompanied by a net increase in the U_{size} (solute atom-dislocation interaction energy) that poses as a formidable energy barrier for dislocation to propagate through the solid-solution because the movement of dislocation in such a material through any given slip plane and slip direction would require climbing a high energy barrier (U). This phenomenon increases the ability of a given alloy to resist plastic deformation, and increases the corresponding hardness (H) of the alloy as shown in Fig. 4 and Fig. 5, where alloys with high U_{size} and alloys that have highly strained lattices exhibit superior H. No clear distinction in the trend of H with lattice strain can be noticed for binary and ternary alloys in Fig. 5 (a) & (b) thereby establishing that entropy or the number of elements has no observable role in determining the hardness, which is in agreement with the work of Wu et al. [14]. Hence, the structural strength of a multi-principal element alloy is primarily dependent on the degree of solid-solution strengthening.

Higher attractive interatomic forces result in higher cohesive energies. Since interatomic forces must be overcome for deformation to occur, we examine the impact of cohesive energy in these alloys as the cohesive forces are signatures of the associated bond strengths in metallic crystals. The cohesive energy (E_{coh}) of a given solid-solution is calculated as [69].

$E^{all}_{coh} = x_A E^{A}_{coh} + x_B E^{B}_{coh} - \Delta H_1$, where ΔH_1 is the formation enthalpy of the alloy A-B, x_A and x_B are the mole fractions of metals A and B, respectively, and E^{A}_{coh}, E^{B}_{coh} and E^{all}_{coh} are the corresponding cohesive energies of the individual components and the alloy. For multicomponent alloys, we extend this formulation to $E^{all}_{coh} = \sum_{i=1}^{i=n} x_i E^{i}_{coh} - \Delta H$, and list the cohesive energies in Table S4 of supplementary information. The formation enthalpy is calculated using Miedema's model for individual binaries [70], which is then extended to multicomponent systems [71]. Fig. 6 (a) illustrates that the variation of E as a function of cohesive energy is approximately linear. Thus, we assert that cohesive forces in the lattice play a dominant role in determining stiffness, and subsequently enhancing the structural properties of certain equiatomic multicomponent alloys.

We further assess the role of number of elements on E of the investigated alloys, by analyzing the variations of E with cohesive energies for binary and ternary BCC alloys exclusively, in Figs. 6 (b-c). A near linear correlation exists between cohesive energy and E of BCC ternary and binary cases albeit with different slopes, which implies that number of

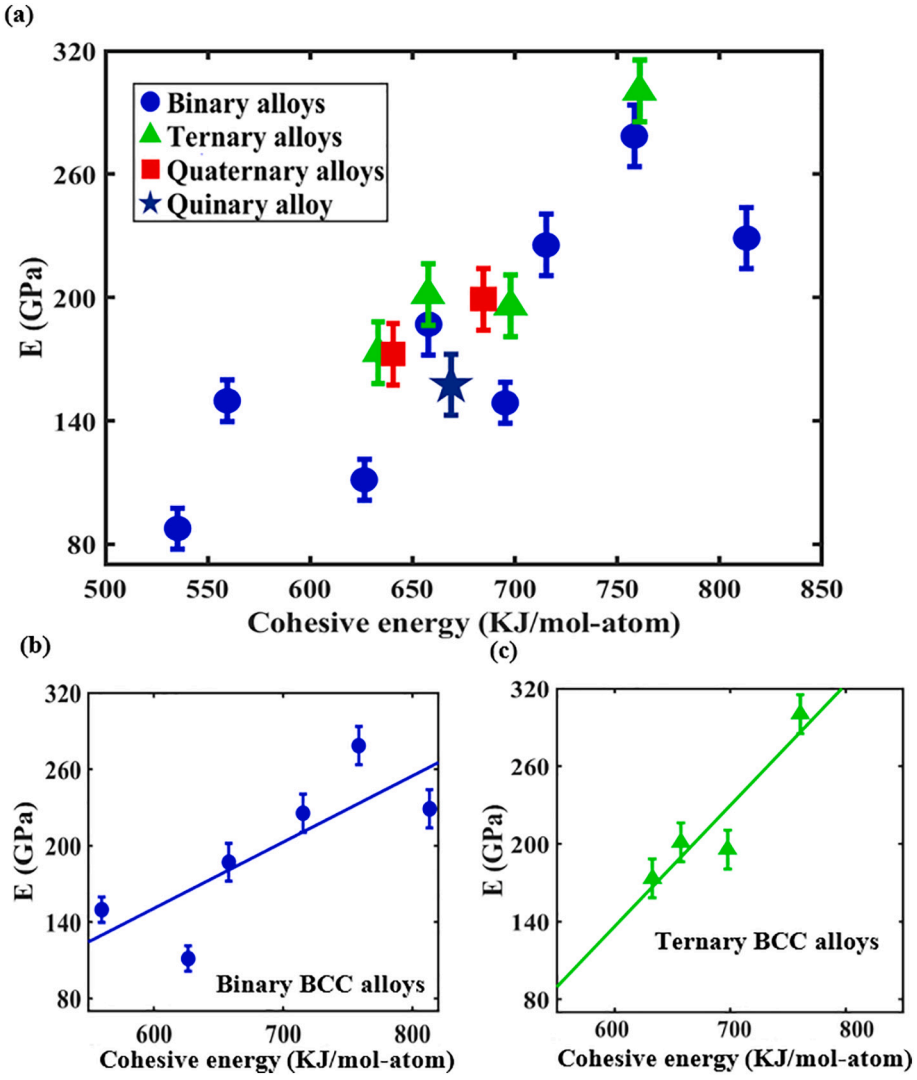

Fig. 6. Young's modulus (E) as a function of the cohesive energy for single-phase multicomponent alloys. (a) The linear correlation suggests that cohesive energy exerts a significant impact on the E of these alloys. To further elaborate on the role of cohesive energies, the the corresponding variation of E with cohesive energies for (b) all binary BCC alloys with $R^2 = 0.63$ and (c) all ternary BCC alloys with $R^2 = 0.85$ are presented, where R^2 measures the goodness of fit. The binary and ternary alloys when considered separately have different slopes for the linear correlation that is suggestive of the relatively minor effect due to entropy resulting from the number of constituent metals in the alloy. As evinced from (b) and (c), the variations in E are reflected by the changes in cohesive energy, as the latter is an indirect measure of the strengths of metallic bonds in the lattice of the alloys. A higher cohesive energy between the atoms in a lattice will require a greater shear force to break the metallic bonds and enable slip. Also, a binary alloy may intrinsically possess a higher cohesive energy than a ternary or quaternary alloy, thereby limiting the effect of relatively higher entropy and outperforming a ternary or quaternary alloy when estimating the structural properties.

elements has a minor effect on structural properties, in that it facilitates classification of the alloys into bands which then show a linear dependence on the cohesive energy with varying slopes. In other words, once we consider a more limited set of alloys with identical configurational entropy or equal number of elements, lattice strain and cohesive energies prove to be a relatively accurate predictor of strength.

In essence, the results reveal that the number of alloying elements does not have an overwhelming effect on structural properties of complex concentrated alloys, but instead, the resultant lattice train generated by the alloying elements can be directly correlated to the hardness. Both the approaches employed to determine the lattice strains suggest that an increase in the lattice strain causes an increase in H of the single-phase solid solution. On the other hand, cohesive energy, which is an indirect metric accounting for the cohesive forces existing in a crystal lattice, varies linearly with E. An alloy composition with lower number of elements may undergo a higher lattice distortion than one with larger number of elements, as predicted by the W—H strain values in, e.g., MoW > MoTiW > MoTaTiW multicomponent alloys. Likewise, a binary equiatomic alloy may possess an enhanced cohesive force between the atoms of its lattice than an equiatomic ternary alloy, for instance, $E_{coh}^{MoW} > E_{coh}^{MoTaTi}$. As such the data presented in the work does not provide any clear evidence that a higher number of alloying elements improves the structural properties in HEAs.

5. Conclusion

Whether the number elements present in a HEA improve the mechanical properties has been an open question which has been only partially addressed in literature with one school of thought stating the number of elements in an HEA improve its structural performance while another stating the opposite. To address this question MoTaTiWZr alloy series was selected to be investigated in this work because the combinations obtained from this series cover all major types of crystal structures while being in single-phase. All possible equiatomic combinations (binary, ternary, quaternary and quinary) were synthesized and investigated for their phases and mechanical properties (E and H). Fifteen (twelve BCC and three HCP alloys were obtained) of the twenty six possible combinations were found to be in single-phase. The experimental measurements of E and H showed that certain binary and ternary alloys had higher E and H values than quaternary and quinary ones. To support our calculations experimentally, it was hypothesized that a HEA with a higher lattice distortion and cohesive energy would be harder and stiffer respectively, than one with low lattice distortion and low cohesive energy. This hypothesis was put to test by quantifying the lattice distortions in terms of the lattice strain and correlating the H values as a function of the lattice strains. Similarly, cohesive energy was calculated and E values were correlated with the cohesive energy. The following conclusions were drawn based on the results:

(1) HEAs with fewer number of metals exhibit higher E and H values than those with higher number of constituents e.g. $H_{MoW} > H_{MoTaW} > H_{MoTaTiW}$ & $E_{MoW} > E_{MoTiW} > E_{MoTaTiWZr}$ (Table S4). Therefore, the number of elements does not play a role in determining the degree of solid solution strengthening.

(2) To theoretically reason our observations we calculate the U_{size} and a roughly linear trend was observed between H and U_{size}. We acknowledge that a more accurate fit could be achieved upon the calculation of the total U, but unavailability of data limits the calculation of $U_{modulus}$, hence total U is not obtainable. To circumvent this obstacle, we use experimental XRD data to correlate H with the lattice strain values and reasonably good linear trend is observed thereby corroborating that lattice distortion is physical quantity which though indirectly, can accurately represent degree of solid solution strengthening.

(3) Cohesive energy also is fairly capable of predicting the stiffness of the lattice as a theoretical quantity that measures bond strengths in HEAs. It is noted that E increases as cohesive energy of the alloy lattice increases. Interestingly, a near linear correlation exists between cohesive energy and *E* of BCC ternary and binary cases albeit with different slopes. From this we conclude that number of elements has a minor effect on structural properties, in that it distinguishes alloys with identical number of elements into bands which then show a linear dependence on the cohesive energy with varying slopes.

Data availability

The data and methods reported in this paper are available from the corresponding author upon reasonable request.

Author contributions

AR: Data curation, Formal analysis, Investigation, Methodology, Visualization; PS: Investigation, Data curation; TB: Investigation, Validation; BK: Investigation. PR: Conceptualization, Formal analysis, Supervision; GB: Conceptualization, Funding acquisition, Project administration. AR, PR, GB: Writing - original draft; All authors: Writing - review & editing.

Declaration of Competing Interest

The authors declare that they have no known competing financial interests or personal relationships that could have appeared to influence the work reported in this paper.

The authors declare the following financial interests/personal relationships which may be considered as potential competing interests:

Acknowledgements

The research was supported by the National Science Foundation (NSF) through the award CMMI-1944040, the NSF Graduate Fellowship Program award # 1842163, and the Ames Laboratory through the U.S. Department of Energy (DOE), Office of Energy Efficiency and Renewable Energy, Advanced Manufacturing Office (AMO) under design project WBS 2.1.0.19. Ames Laboratory is operated by Iowa State University for the U.S. DOE under contract DE-AC02-07CH11358.

Appendix A. Supplementary data

Supplementary data to this article can be found online at https://doi.org/10.1016/j.matchar.2021.110877.

References

[1] J.W. Yeh, S.K. Chen, S.J. Lin, J.Y. Gan, T.S. Chin, T.T. Shun, C.H. Tsau, S.Y. Chang, Nanostructured high-entropy alloys with multiple principal elements: novel alloy design concepts and outcomes, Adv. Eng. Mater. 6 (2004) 299–303.
[2] O.N. Senkov, D.B. Miracle, K.J. Chaput, J.-P. Couzinie, Development and exploration of refractory high entropy alloys—a review, J. Mater. Res. 33 (2018) 3092–3128.
[3] J. Rickman, H. Chan, M. Harmer, J. Smeltzer, C. Marvel, A. Roy, G. Balasubramanian, Materials informatics for the screening of multi-principal elements and high-entropy alloys, Nat. Commun. 10 (2019) 2618.
[4] O.N. Senkov, G. Wilks, J. Scott, D.B. Miracle, Mechanical properties of Nb25Mo25Ta25W25 and V20Nb20Mo20Ta20W20 refractory high entropy alloys, Intermetallics 19 (2011) 698–706.
[5] O.A. Waseem, H.J. Ryu, Combinatorial synthesis and analysis of AlxTayVz-Cr20Mo20Nb20Ti20Zr10 and Al10CrMoxNbTiZr10 refractory high-entropy alloys: oxidation behavior, J. Alloys Compd. 828 (2020) 154427.
[6] Y. Chou, Y. Wang, J. Yeh, H. Shih, Pitting corrosion of the high-entropy alloy Co1. 5CrFeNi1. 5Ti0. 5Mo0. 1 in chloride-containing sulphate solutions, Corros. Sci. 52 (2010) 3481–3491.
[7] E. Osei-Agyemang, G. Balasubramanian, Surface oxidation mechanism of a refractory high-entropy alloy, NPJ Mater. Degrad. 3 (2019) 20.
[8] Z. Wu, H. Bei, G.M. Pharr, E.P. George, Temperature dependence of the mechanical properties of equiatomic solid solution alloys with face-centered cubic crystal structures, Acta Mater. 81 (2014) 428–441.
[9] F. Průša, M. Cabibbo, A. Šenková, V. Kučera, Z. Veselka, A. Školáková, D. Vojtěch, J. Cibulková, J. Čapek, High-strength ultrafine-grained CoCrFeNiNb high-entropy alloy prepared by mechanical alloying: properties and strengthening mechanism, J. Alloys Compd. 835 (2020) 155308.
[10] M. Gianelle, A. Kundu, K. Anderson, A. Roy, G. Balasubramanian, H.M. Chan, A novel ceramic derived processing route for multi-principal element alloys, Mater. Sci. Eng. A 793 (2020) 139892.
[11] J. Brechtl, S. Chen, C. Lee, Y. Shi, R. Feng, X. Xie, D. Hamblin, A.M. Coleman, B. Straka, H. Shortt, A review of the serrated-flow phenomenon and its role in the deformation behavior of high-entropy alloys, Metals 10 (2020) 1101.
[12] J.-W. Yeh, Physical metallurgy of high-entropy alloys, Jom 67 (2015) 2254–2261.
[13] A. Zaddach, C. Niu, C. Koch, D. Irving, Mechanical properties and stacking fault energies of NiFeCrCoMn high-entropy alloy, Jom 65 (2013) 1780–1789.
[14] Z. Wu, H. Bei, F. Otto, G.M. Pharr, E.P. George, Recovery, recrystallization, grain growth and phase stability of a family of FCC-structured multi-component equiatomic solid solution alloys, Intermetallics 46 (2014) 131–140.
[15] G. Salishchev, M. Tikhonovsky, D. Shaysultanov, N. Stepanov, A. Kuznetsov, I. Kolodiy, A. Tortika, O. Senkov, Effect of Mn and V on structure and mechanical properties of high-entropy alloys based on CoCrFeNi system, J. Alloys Compd. 591 (2014) 11–21.
[16] D. Zhang, Y. Mao, Y. Li, J. Li, M. Yuan, J. Lin, Effect of ternary alloying elements on microstructure and superelastictity of Ti–Nb alloys, Mater. Sci. Eng. A 559 (2013) 706–710.
[17] A. Roy, T. Babuska, B. Krick, G. Balasubramanian, Machine learned feature identification for predicting phase and Young's modulus of low-, medium-and high-entropy alloys, Scr. Mater. 185 (2020) 152–158.
[18] B.S. Murty, J.-W. Yeh, S. Ranganathan, P. Bhattacharjee, High-Entropy Alloys, Elsevier, 2019.
[19] C.-Y. Hsu, C.-C. Juan, W.-R. Wang, T.-S. Sheu, J.-W. Yeh, S.-K. Chen, On the superior hot hardness and softening resistance of AlCoCrxFeMo0. 5Ni high-entropy alloys, Mater. Sci. Eng. A 528 (2011) 3581–3588.
[20] K.-Y. Tsai, M.-H. Tsai, J.-W. Yeh, Sluggish diffusion in co–Cr–Fe–Mn–Ni high-entropy alloys, Acta Mater. 61 (2013) 4887–4897.
[21] J. Dąbrowa, M. Danielewski, State-of-the-art diffusion studies in the high entropy alloys, Metals 10 (2020) 347.
[22] D. Beke, G. Erdélyi, On the diffusion in high-entropy alloys, Mater. Lett. 164 (2016) 111–113.
[23] L. Owen, E. Pickering, H. Playford, H. Stone, M. Tucker, N. Jones, An assessment of the lattice strain in the CrMnFeCoNi high-entropy alloy, Acta Mater. 122 (2017) 11–18.
[24] Z. Lei, X. Liu, Y. Wu, H. Wang, S. Jiang, S. Wang, X. Hui, Y. Wu, B. Gault, P. Kontis, Enhanced strength and ductility in a high-entropy alloy via ordered oxygen complexes, Nature 563 (2018) 546–550.
[25] Y.-J. Liang, L. Wang, Y. Wen, B. Cheng, Q. Wu, T. Cao, Q. Xiao, Y. Xue, G. Sha, Y. Wang, High-content ductile coherent nanoprecipitates achieve ultrastrong high-entropy alloys, Nat. Commun. 9 (2018) 1–8.
[26] Y. Lu, Y. Dong, S. Guo, L. Jiang, H. Kang, T. Wang, B. Wen, Z. Wang, J. Jie, Z. Cao, A promising new class of high-temperature alloys: eutectic high-entropy alloys, Sci. Rep. 4 (2014) 6200.
[27] P. Singh, A. Sharma, A.V. Smirnov, M.S. Diallo, P.K. Ray, G. Balasubramanian, D. D. Johnson, Design of high-strength refractory complex solid-solution alloys, NPJ Computat. Mater. 4 (2018) 16.
[28] S. Luo, Y. Liao, Y. Tsai, Wear characteristics in turning high hardness alloy steel by ceramic and CBN tools, J. Mater. Process. Technol. 88 (1999) 114–121.
[29] W.D. Callister, D.G. Rethwisch, Materials Science and Engineering, John wiley & sons NY, 2011.
[30] T. Degen, M. Sadki, E. Bron, U. Konig, G. Nenert, The HighScore suite, Powder Diffract. 29 (2014) S13–S18.
[31] W.C. Oliver, G.M. Pharr, An improved technique for determining hardness and elastic modulus using load and displacement sensing indentation experiments, J. Mater. Res. 7 (1992) 1564–1583.

[32] J. English, Binary and Ternary Phase Diagrams of Columbium, Molybdenum, Tantalum, and Tungsten, Defense Metals Information Center, Battelle Memorial Institute, 1961.
[33] W.P. Huhn, M. Widom, Prediction of A2 to B2 phase transition in the high-entropy alloy Mo-Nb-ta-W, Jom 65 (2013) 1772–1779.
[34] M. Morinaga, 1.3 - The molecular orbital approach and its application to biomedical titanium alloy design, in: F.H. Froes, M. Qian (Eds.), Titanium in Medical and Dental Applications, Woodhead Publishing, 2018, pp. 39–64.
[35] D.R. Olander, A.T. Motta, A new book:'light-water reactor materials', Nucl. Eng. Technol. 37 (2005) 309–316.
[36] M.H. Read, C. Altman, A new structure in tantalum thin films, Appl. Phys. Lett. 7 (1965) 51–52.
[37] X. Yang, Y. Zhang, Prediction of high-entropy stabilized solid-solution in multi-component alloys, Mater. Chem. Phys. 132 (2012) 233–238.
[38] C. Varvenne, A. Luque, W.A. Curtin, Theory of strengthening in fcc high entropy alloys, Acta Mater. 118 (2016) 164–176.
[39] T. Egami, Y. Waseda, Atomic size effect on the formability of metallic glasses, J. Non-Cryst. Solids 64 (1984) 113–134.
[40] H. Chen, A. Kauffmann, S. Laube, I.-C. Choi, R. Schwaiger, Y. Huang, K. Lichtenberg, F. Müller, B. Gorr, H.-J. Christ, Contribution of lattice distortion to solid solution strengthening in a series of refractory high entropy alloys, Metall. Mater. Trans. A 49 (2018) 772–781.
[41] Y. Zhang, X. Yang, P. Liaw, Alloy design and properties optimization of high-entropy alloys, Jom 64 (2012) 830–838.
[42] Z. Wang, Y. Huang, Y. Yang, J. Wang, C. Liu, Atomic-size effect and solid solubility of multicomponent alloys, Scr. Mater. 94 (2015) 28–31.
[43] Z. Wang, W. Qiu, Y. Yang, C. Liu, Atomic-size and lattice-distortion effects in newly developed high-entropy alloys with multiple principal elements, Intermetallics 64 (2015) 63–69.
[44] G. Pharr, W. Oliver, Nanoindentation of silver-relations between hardness and dislocation structure, J. Mater. Res. 4 (1989) 94–101.
[45] C. Chen, A. Hendrickson, Dislocation etch pits in silver, J. Appl. Phys. 42 (1971) 2208–2215.
[46] T.H. Courtney, Mechanical Behavior of Materials, Waveland Press, 2005.
[47] O. Senkov, D. Miracle, A topological model for metallic glass formation, J. Non-Cryst. Solids 317 (2003) 34–39.
[48] E.S. Pacheco, T. Mura, Influence of shear moduli and lattice parameters on the equilibrium of a screw dislocation, J. Compos. Mater. 3 (1969) 664–675.
[49] R.L. Fleischer, Substitutional solution hardening, Acta Metall. 11 (1963) 203–209.
[50] R. Naorem, A. Gupta, S. Mantri, G. Sethi, K. ManiKrishna, R. Pala, K. Balani, A. Subramaniam, A critical analysis of the X-ray diffraction intensities in concentrated multicomponent alloys, Int. J. Mater. Res. 110 (2019) 393–405.
[51] Q. He, Y. Yang, On lattice distortion in high entropy alloys, Front. Mater. 5 (2018).
[52] Z. Wang, Q. Fang, J. Li, B. Liu, Y. Liu, Effect of lattice distortion on solid solution strengthening of BCC high-entropy alloys, J. Mater. Sci. Technol. 34 (2018) 349–354.
[53] M. Turchanin, P. Agraval, Cohesive energy, properties, and formation energy of transition metal alloys, Powder Metal. Metal Ceram. 47 (2008) 26–39.
[54] J.-W. Yeh, S.-Y. Chang, Y.-D. Hong, S.-K. Chen, S.-J. Lin, Anomalous decrease in X-ray diffraction intensities of cu–Ni–Al–co–Cr–Fe–Si alloy systems with multi-principal elements, Mater. Chem. Phys. 103 (2007) 41–46.
[55] S. Praveen, B. Murty, R.S. Kottada, Alloying behavior in multi-component AlCoCrCuFe and NiCoCrCuFe high entropy alloys, Mater. Sci. Eng. A 534 (2012) 83–89.
[56] D. Oleszak, A. Antolak-Dudka, T. Kulik, High entropy multicomponent WMoNbZrV alloy processed by mechanical alloying, Mater. Lett. 232 (2018) 160–162.
[57] R.A. Young, The Rietveld Method, International Union of Crystallography, 1993.
[58] L. Lutterotti, MAUD CPD newsletter (IUCr), No. 24, December, 2000.
[59] G. Williamson, W. Hall, X-ray line broadening from filed aluminium and wolfram, Acta Metall. 1 (1953) 22–31.
[60] N. Popa, The (hkl) dependence of diffraction-line broadening caused by strain and size for all Laue groups in Rietveld refinement, J. Appl. Crystallogr. 31 (1998) 176–180.
[61] B.H. Toby, R factors in Rietveld analysis: how good is good enough? Powder Diffract. 21 (2006) 67–70.
[62] M. Karolus, E. Łągiewka, Crystallite size and lattice strain in nanocrystalline Ni–Mo alloys studied by Rietveld refinement, J. Alloys Compd. 367 (2004) 235–238.
[63] P. Scherrer, Bestimmung der Größe und der inneren Struktur von Kolloidteilchen mittels Röntgenstrahlen, Nachrichten von der Gesellschaft der Wissenschaften zu Göttingen, Mathematisch-Physikalische Klasse, 1918.
[64] A.W. Burton, K. Ong, T. Rea, I.Y. Chan, On the estimation of average crystallite size of zeolites from the Scherrer equation: a critical evaluation of its application to zeolites with one-dimensional pore systems, Microporous Mesoporous Mater. 117 (2009) 75–90.
[65] K.V.R. Yendrapati Taraka Prabhu, Vemula Sesha Sai Kumar, Bandla Siva Kumari, X-ray analysis by williamson-hall and size-strain plot methods of ZnO nanoparticles with fuel variation, World J. Nano Sci. Eng. 4 (1) (2014) 8.
[66] J.W. Yeh, Y.L. Chen, S.J. Lin, S.K. Chen, High-entropy alloys – a new era of exploitation, Mater. Sci. Forum 560 (2007) 1–9.
[67] F. Wang, Y. Zhang, G. Chen, Atomic packing efficiency and phase transition in a high entropy alloy, J. Alloys Compd. 478 (2009) 321–324.
[68] Z. Wang, Q.H. Fang, J. Li, B. Liu, Y. Liu, Effect of lattice distortion on solid solution strengthening of BCC high-entropy alloys, J. Mater. Sci. Technol. 34 (2018) 349–354.
[69] C. Li, J.L. Hoe, P. Wu, Empirical correlation between melting temperature and cohesive energy of binary laves phases, J. Phys. Chem. Solids 64 (2003) 201–212.
[70] A. Miedema, F. De Boer, R. Boom, Model predictions for the enthalpy of formation of transition metal alloys, Calphad 1 (1977) 341–359.
[71] A. Takeuchi, A. Inoue, Calculations of mixing enthalpy and mismatch entropy for ternary amorphous alloys, Mater. Trans. JIM 41 (2000) 1372–1378.